

Infrared Study of Sapphire α -Al₂O₃ by Small-Angle Oblique-Incidence Reflectometry

Yuji KUMAGAI*, Hiroyuki YOKOI, Hitoshi TAMPO¹, Yoshinori TABATA², and Noritaka KURODA^{‡§}

*Department of Materials Science and Engineering, Graduate School of Science and Technology,
Kumamoto University, Kumamoto 860-8555, Japan*

¹*National Institute of Advanced Industrial Science and Technology (AIST), Tsukuba 305-8568, Japan*

²*Faculty of Pharmaceutical Sciences, Hokuriku University, Kanazawa 920-1181, Japan*

Abstract

Infrared properties of the multimode polar optical phonons in sapphire have been studied by the small-angle oblique-incidence reflectometry (SAOIR) using the a - and c -face of the crystal. It is found that the reststrahlen reflection accompanies the total reflection due to Snell's law and the null reflection due to Brewster's law in the form of line structures at frequencies very close to longitudinal optical (LO) phonons. The analysis of the observations in terms of Gervais and Piriou's four-parameter semi-quantum oscillator model yields the frequencies and damping energies of all modes of the polar optical phonons. In addition, three weak bands which are allowed for $E\parallel c$ and ascribed to the multiphonon absorptions are observed on the wing of the reststrahlen band of an A_{2u} mode.

KEYWORDS: small-angle oblique-incidence infrared reflection, Brewster's null reflection, Snell's total reflection, LO phonon, multiphonon absorption, sapphire

1. Introduction

The rhombohedral primitive unit cell of the α -corundum structure of sapphire contains two units of Al₂O₃, and thus yields more than one mode of optical lattice vibration for polarizations both parallel and perpendicular to the c -axis. Because the rhombohedral lattice has the inversion symmetry, all the polar optical modes are active for the infrared dipole transition but inactive for the Raman scattering. The overall structure of those infrared-active normal modes has been clarified by the pioneering works of Mistuishi *et al.*,¹⁾ and Barker²⁾. Gervais and Piriou³⁾ have paid attention to the anharmonic coupling between the normal modes, putting forward the four-parameter semi-quantum (FPSQ) oscillator model to describe the one-phonon residual-ray spectrum, that is, the reststrahlen spectrum, taken from the c -face of the crystal. To date, the FPSQ model has been recognized to be valid in a variety of materials including binary compounds.

In addition to its various favorable properties, the trigonal structure and the proximity of its lattice constant to that of GaN have promoted the c -face sapphire to be used as the substrate for the light-emitting diodes and laser diodes of GaN-based group III-nitrides. The a -face sapphire also works as

the substrate for molecular beam epitaxy of ZnO well.⁴⁾ Accordingly, for the last 15 years there has been a continuing interest in the infrared lattice-vibrational properties of semiconductor-sapphire composites of GaN/ c -sapphire⁶⁻¹⁰⁾, MgZnO/ c -sapphire¹¹⁾, ZnO/ a -sapphire¹²⁾, AlN/ c -sapphire¹³⁾, and InAlGaN/ c -sapphire¹⁴⁾. The properties of the infrared-active normal modes of sapphire itself have also been studied extensively¹⁵⁻¹⁸⁾.

Another interesting aspect of the infrared properties of sapphire is the multiphonon absorption that can be presumed from the anharmonicity of normal modes. As argued by Gervais and Piriou in their aforementioned study, the reflectivity spectrum for $E\perp c$ at frequencies below 1000 cm⁻¹ can be explained in terms of the one-phonon transition alone, where E is the electric-field vector of radiation, and c is the c -axis of the crystal. However, there appears a two-phonon absorption band between 1400 and 1500 cm⁻¹ for $E\parallel c$, and besides, a weak higher-order multiphonon absorption band decaying exponentially with increasing frequency from about 1500 cm⁻¹ is observed for both $E\perp c$ and $E\parallel c$.¹⁹⁾

In the present work we carry out the systematic study of infrared small-angle oblique-incidence reflectometry²⁰⁾ (SAOIR) in sapphire using the a - and c -face crystals. The SAOIR technique makes use of

the fact that the null reflection due to Brewster's law and the total reflection due to Snell's law occur consecutively in the frequency region of the longitudinal optical waves when the linearly-polarized light beam is incident slightly obliquely from normal to the crystal surface. The infrared SAOIR has been adopted successfully for characterizing polar optical phonons in ZnO,²¹⁾ where the experiment has been performed for the c -face of bulk crystals. Similarly, except for the study of Barker²⁾ on a fusion crystal of ruby, α -Al₂O₃:Cr³⁺, most of the previous infrared experiments on the bulk sapphire are restricted to the crystals with the c -face. Therefore, only a little information is available on the multiphonon absorption for $\mathbf{E}||c$ in the long-wave region. In the present study, we examine the SAOIR properties of polar optical phonons of sapphire by measuring the spectrum for all the principal configurations with the a - and c -face of the crystal. At the same time, we search for the multiphonon absorption in the region of the long-wave, reststrahlen reflection for $\mathbf{E}||c$. For these purposes the theoretical background of SAOIR for the a - and c -face crystals of sapphire is surveyed in §2. The experimental procedure is described in §3 and the results are presented and discussed in §4.

2. Theoretical Background of SAOIR of Sapphire

We deal with the reflection of linearly polarized infrared light from the principal faces of the sapphire crystal which is oriented as shown in Fig. 1. The crystal axes are set parallel to the axes x_i 's of $i = 1, 2,$ or 3 of the Cartesian coordinates of the laboratory system. Let the plane of incidence stand vertical to the crystal face along the x_2 direction. Then the experimental configurations are specified by the polarization s or p , the direction x_2 , and the direction x_3 normal to the crystal face. Here we represent the configurations as sx_2x_3 or px_2x_3 , expressing x_2 and x_3 in terms of crystal axes a and c . Since a uniaxial crystal is optically isotropic within the plane normal to the c -axis, we may write any direction within the c -face as a . Consequently, the principal configurations are represented as $sac, pac, saa, paa, sca,$ and pca .

The α -corundum structure provides uniaxial birefringence for sapphire. Expressing the principal components of the dielectric tensor for the directions of the electric field of light parallel to the a and c axes as $\varepsilon_{\perp}(\omega)$ and $\varepsilon_{\parallel}(\omega)$, respectively, at the frequency ω , and taking the angle of incidence of light as θ , the reflectivities in the six principal configurations are

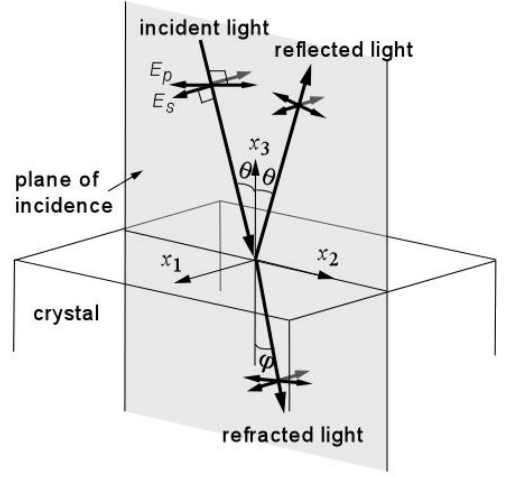


Fig. 1 Optical configuration for the measurement of oblique-incidence reflection. Arrows E_s and E_p denote s - and p -polarized electric fields of light, respectively.

given as follows:^{20, 22)}

(1) sac

$$R_{sac} = \left| \frac{\cos \theta - \sqrt{\varepsilon_{\perp}(\omega) - \sin^2 \theta}}{\cos \theta + \sqrt{\varepsilon_{\perp}(\omega) - \sin^2 \theta}} \right|^2, \quad (1a)$$

(2) pac

$$R_{pac} = \left| \frac{\sqrt{\varepsilon_{\parallel}(\omega)\varepsilon_{\perp}(\omega)} \cos \theta - \sqrt{\varepsilon_{\parallel}(\omega) - \sin^2 \theta}}{\sqrt{\varepsilon_{\parallel}(\omega)\varepsilon_{\perp}(\omega)} \cos \theta + \sqrt{\varepsilon_{\parallel}(\omega) - \sin^2 \theta}} \right|^2, \quad (1b)$$

(3) saa

$$R_{saa} = \left| \frac{\cos \theta - \sqrt{\varepsilon_{\parallel}(\omega) - \sin^2 \theta}}{\cos \theta + \sqrt{\varepsilon_{\parallel}(\omega) - \sin^2 \theta}} \right|^2, \quad (1c)$$

(4) paa

$$R_{paa} = \left| \frac{\varepsilon_{\perp}(\omega) \cos \theta - \sqrt{\varepsilon_{\perp}(\omega) - \sin^2 \theta}}{\varepsilon_{\perp}(\omega) \cos \theta + \sqrt{\varepsilon_{\perp}(\omega) - \sin^2 \theta}} \right|^2, \quad (1d)$$

(5) sca

$$R_{sca} = \left| \frac{\cos \theta - \sqrt{\varepsilon_{\perp}(\omega) - \sin^2 \theta}}{\cos \theta + \sqrt{\varepsilon_{\perp}(\omega) - \sin^2 \theta}} \right|^2 = R_{sac}, \quad (1e)$$

(6) pca

$$R_{pca} = \left| \frac{\sqrt{\varepsilon_{\parallel}(\omega)\varepsilon_{\perp}(\omega)} \cos \theta - \sqrt{\varepsilon_{\perp}(\omega) - \sin^2 \theta}}{\sqrt{\varepsilon_{\parallel}(\omega)\varepsilon_{\perp}(\omega)} \cos \theta + \sqrt{\varepsilon_{\perp}(\omega) - \sin^2 \theta}} \right|^2. \quad (1f)$$

Table I. Frequencies (cm^{-1}) of polar optical modes in sapphire. Numbers in parentheses are the damping energies (cm^{-1}). For the frequency and damping energy of the present work, the errors are $\pm 0.2 \text{ cm}^{-1}$ for LO_{\parallel}^1 , LO_{\parallel}^2 and LO_{\perp}^2 , and $\pm 0.3 \text{ cm}^{-1}$ and $\pm 0.5 \text{ cm}^{-1}$, respectively, for other modes.

Mode		Present work	Yu et al. ¹⁸⁾	Schubert et al. ¹⁷⁾	Thomas et al. ¹⁶⁾
A_{2u}^1	TO_{\parallel}^1	398.0 (5.7)	397.2(1.5)	397.5(5.3)	399.5(8.0)
	LO_{\parallel}^1	511.0 (1.5)	510.9(1.2)	510.8(1.1)	516.0(8.0)
A_{2u}^2	TO_{\parallel}^2	583.0(2.5)	583.0(1.5)	582.4(3.0)	584.0(20)
	LO_{\parallel}^2	879.4(18.5)	878.6(19.2)	881.1(15.4)	875.5(20)
E_u^1	TO_{\perp}^1	384.6(4.8)	385.1(2.7)	384.9(3.3)	384.3(4.2)
	LO_{\perp}^1	387.7(4.8)	387.5(2.8)	387.6(3.1)	387.2(4.2)
E_u^2	TO_{\perp}^2	439.3(4.8)	439.4(3.1)	439.1(3.1)	438.9(2.6)
	LO_{\perp}^2	481.2(1.8)	481.5(2.1)	481.6(1.9)	482.1(2.6)
E_u^3	TO_{\perp}^3	569.5(4.5)	569.0(4.5)	569.0(4.7)	568.2(6.8)
	LO_{\perp}^3	629.2(6.5)	629.9(6.5)	629.5(5.9)	629.9(6.8)
E_u^4	TO_{\perp}^4	633.5(5.2)	634.1(4.9)	633.6(5.0)	633.6(6.3)
	LO_{\perp}^4	908.5(20.0)	906.5(19.3)	906.6(14.7)	903.0(6.3)

We have $R_{sca} = R_{sac}$, as indicated by eq. (1e), because of the uniaxial symmetry of the crystal structure of sapphire.

The α -corundum structure of sapphire belongs to the D_{3d} point group and yields the following normal modes of lattice vibration:²⁾

$$\Gamma = 2A_{1g} + 2A_{1u} + 3A_{2g} + 3A_{2u} + 5E_g + 5E_u. \quad (2)$$

One A_{2u} and one E_u representations are acoustic modes and the other two representations of A_{2u} and four representations of E_u are infrared-active optical modes polarized parallel and perpendicular to the c -axis, respectively. Each infrared-active optical mode produces a pair of branches of the transverse optical (TO) and longitudinal optical (LO) phonons. In Gervais and Piriou's FPSQ oscillator model³⁾, the principal dielectric functions are given by

$$\varepsilon_{\parallel(\perp)}(\omega) = \varepsilon_{\infty\parallel(\perp)} \prod_j \frac{\omega_{\text{LO}_{\parallel(\perp)}^j}^2 - \omega^2 - i\gamma_{\text{LO}_{\parallel(\perp)}^j} \omega}{\omega_{\text{TO}_{\parallel(\perp)}^j}^2 - \omega^2 - i\gamma_{\text{TO}_{\parallel(\perp)}^j} \omega}, \quad (3)$$

where ε_{∞} is the optical dielectric constant, $\omega_{\text{LO(TO)}}$ is the frequency of the LO(TO) phonon, and $\gamma_{\text{LO(TO)}}$ is the damping energy of the LO(TO) phonon. Two LO_{\parallel}^j (TO_{\parallel}^j)'s with $j=1$ and 2 signify two LO(TO) phonons of the A_{2u} modes, whereas four LO_{\perp}^j (TO_{\perp}^j)'s with $j = 1 - 4$ signify four LO(TO) phonons

of the E_u modes.

In this section, for clarity of the physical picture, we assume that all the TO and LO phonons have negligible damping, namely, $\gamma_{\text{TO}_{\parallel(\perp)}^j} = \gamma_{\text{LO}_{\parallel(\perp)}^j} = 0$, and therefore, $\varepsilon_{\parallel}(\omega)$ and $\varepsilon_{\perp}(\omega)$ are real. The theoretical curves of R are calculated by using phonon frequencies obtained in this study and listed in Table I: Details of the experimental derivation of the phonon frequencies are described in §4. Here we take θ to be 10° in accord with our experiment, and employ $\varepsilon_{\infty\perp} = 3.064$ and $\varepsilon_{\infty\parallel} = 3.038$ determined by Harman *et al.*¹⁵⁾

Figures 2, 3, and 4 show the calculated curves of R for sac and pac , sca and paa , and saa and pca , respectively. The s and p spectra displayed together in respective Figures are the ones which become identical when $\theta = 0$. Figures 2(a), 3(a), and 4(a) show the spectra over the whole range of frequency covering the six normal modes; Figs. 2(b)-2(f), Figs. 3(b)-3(f), and Figs. 4(b)-4(f) show the close-up of the spectra around every LO phonon.

From Table I we have $\omega_{\text{LO}} > \omega_{\text{TO}}$ for any modes. Thus as evident from eq. (3), for ω above every TO phonon, $\varepsilon_{\parallel(\perp)}(\omega)$ increases monotonically with a zero at the frequency of the conjugate LO mode. The small $\varepsilon_{\parallel(\perp)}(\omega)$ just around every LO phonon is crucial to Snell's total reflection (STR) and Brewster's null reflection (BNR). If we write the dielectric function of the crystal responsible for the refracted light as $\varepsilon(\omega)$,

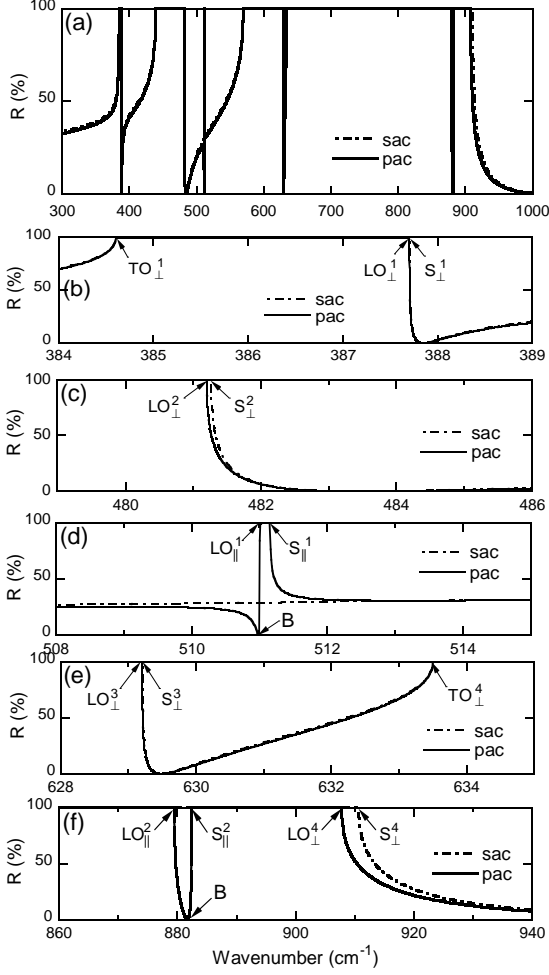


Fig. 2 Calculated SAOIR spectra of sapphire at $\theta = 10^\circ$ in the configurations *sac* (dash-dotted lines) and *pac* (solid lines). In the calculation, phonons are assumed to undergo no damping. Arrows show the singular points due to LO phonons $LO_{\parallel(\perp)}$, polaritons $S'_{\parallel(\perp)}$, and Brewster's null reflections B. The topmost figure (a) is the spectrum in the whole range from 300 to 1000 cm^{-1} , while lower figures (b)-(f) are the close-ups around respective singular points.

from Snell's law on the refraction angle φ we have

$$\varepsilon(\omega) \sin^2 \varphi = \sin^2 \theta. \quad (4)$$

When $\varepsilon(\omega)$ is negative the incident light cannot be transmitted into the crystal, and therefore the incident light is totally reflected. It is apparent from eq. (4) that if $\varepsilon(\omega)$ is positive but yet smaller than $\sin^2 \theta$, the incident light is still totally reflected, giving rise to STR. The usual, partial reflection takes place in a frequency region satisfying $\varepsilon(\omega) > \sin^2 \theta$. To quantify the STR, we write hereafter the ordinary and extraordinary polariton states of $\varepsilon_{\perp}(\omega) = \sin^2 \theta$ and $\varepsilon_{\parallel}(\omega) = \sin^2 \theta$ as S_{\perp} and S_{\parallel} , and their frequencies as $\omega_{S_{\perp}}$ and $\omega_{S_{\parallel}}$, respectively. It follows from eq.(3) that $\omega_{S_{\parallel(\perp)}} > \omega_{LO_{\parallel(\perp)}}$ for any modes of LO phonons. In Table II listed are the values of $\omega_{S_{\parallel(\perp)}} - \omega_{LO_{\parallel(\perp)}}$ for $\theta =$

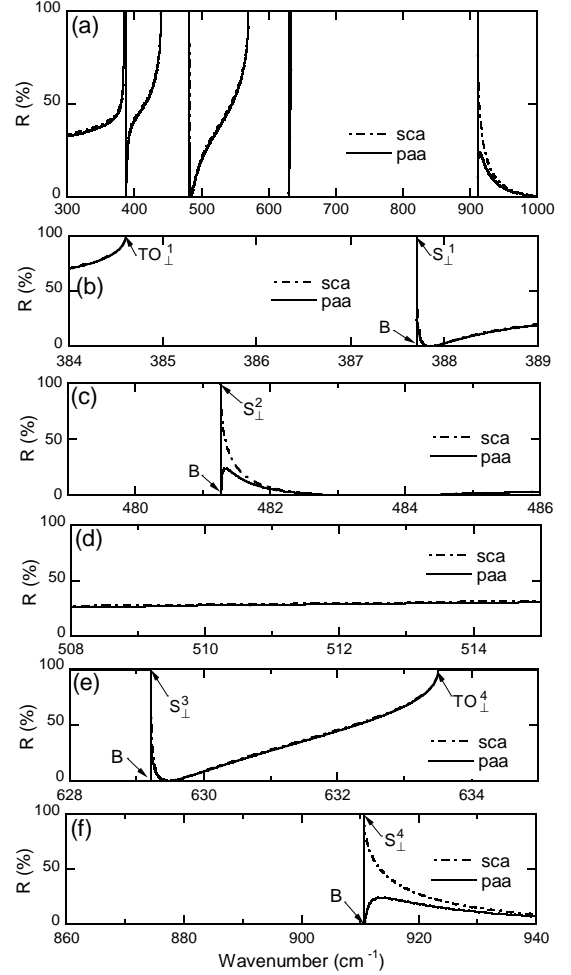


Fig. 3 Calculated SAOIR spectra of sapphire at $\theta = 10^\circ$ in the configurations *sca* (dash-dotted lines) and *paa* (solid lines). For other explanations, see the caption of Fig. 2.

10° . The frequency difference ranges from nearly null of $S_{\perp}^1 - LO_{\perp}^1$ to 2.89 cm^{-1} of $S_{\perp}^2 - LO_{\perp}^2$.

For configurations *sac*, *sca*, and *paa*, the infrared light is ordinary ray, and therefore, $\varepsilon(\omega)$ is given by

$$\varepsilon(\omega) = \varepsilon_{\perp}(\omega). \quad (5)$$

Thus S_{\perp}^{1-4} form the upper bound of STR rising from LO_{\perp}^{1-4} of four E_u modes, as seen in Figs. 2(b), 2(c), 2(e), and 2(f) for *sac*, and in Figs. 3(b), 3(c), 3(e), and 3(f) for *sca* and *paa*. In the configuration *saa* the infrared light is extraordinary ray with the electric field directed parallel to the c -axis regardless of θ . Therefore

$$\varepsilon(\omega) = \varepsilon_{\parallel}(\omega), \quad (6)$$

and thus STR occurs in the spectral range from LO_{\parallel} to S_{\parallel} around the LO phonon edges of two A_{2u} modes, as shown in Figs. 4(d) and 4(f). In configurations *pac* and *pca*, since the electric field of the infrared light has the

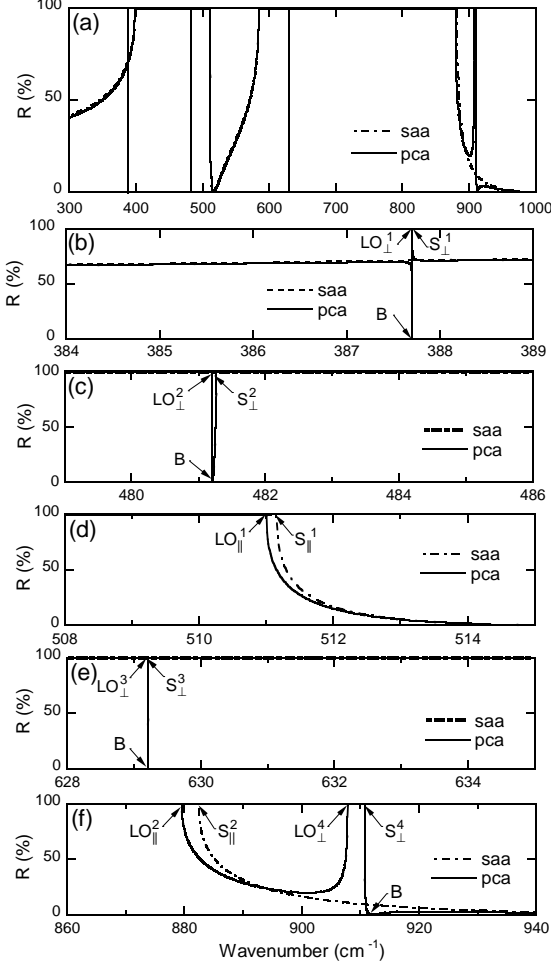


Fig. 4 Calculated SAOIR spectra of sapphire at $\theta = 10^\circ$ in the configurations *saa* (dash-dotted lines) and *pca* (solid lines). For other explanations, see the caption of Fig. 2.

c -component, the light is extraordinary ray, as well. Representing the angle that the wave vector of an extraordinary ray makes against the c -axis as ϕ , $\varepsilon(\omega)$ is given by Fresnel's equation

$$\frac{1}{\varepsilon(\omega)} = \frac{\sin^2 \phi}{\varepsilon_{\parallel}(\omega)} + \frac{\cos^2 \phi}{\varepsilon_{\perp}(\omega)}. \quad (7)$$

We have $\phi = \varphi$ for *pac* and $\phi = \pi/2 - \varphi$ for *pca*, so that with the aid of eq. (4) eq. (7) may be rewritten into

$$\varepsilon(\omega) = \varepsilon_{\perp}(\omega) + \sin^2 \theta - \frac{\varepsilon_{\perp}(\omega)}{\varepsilon_{\parallel}(\omega)} \sin^2 \theta, \quad (8)$$

for *pac*, and into

$$\varepsilon(\omega) = \varepsilon_{\parallel}(\omega) + \sin^2 \theta - \frac{\varepsilon_{\parallel}(\omega)}{\varepsilon_{\perp}(\omega)} \sin^2 \theta, \quad (9)$$

for *pca*. Equation (8) tells us that in *pac* LO_{\perp} and S_{\parallel} give $\varepsilon(\omega) = \sin^2 \theta$ and are responsible for the upper or lower bounds of STR, as seen in Figs. 2(b)-2(f), while

Table II. Frequency difference (cm^{-1}) of the polariton $S_{\parallel,\perp}^j$ from $LO_{\parallel,\perp}^j$.

S_{\parallel}^1	S_{\parallel}^2	S_{\perp}^1	S_{\perp}^2	S_{\perp}^3	S_{\perp}^4
0.15	2.89	< 0.01	0.07	0.01	2.85

according to eq. (9), in *pca* LO_{\parallel} and S_{\perp} give $\varepsilon(\omega) = \sin^2 \theta$ and are responsible for the upper or lower bounds of STR, as seen in Figs. 4(b)-4(f).

The most remarkable aspect of SAOIR is Brewster's null reflection (BNR) that occurs in the p -polarization in the close vicinity of every LO phonon mode polarized normal to the crystal face.^{20,21} It turns out from eqs. (1b), (1d), and (1f) that the frequencies of those BNR are the solutions of the following equations:²³⁾

$$\frac{\varepsilon_{\perp}(\omega) - 1}{\varepsilon_{\parallel}(\omega) - 1} \varepsilon_{\parallel}(\omega) = \tan^2 \theta, \quad (10a)$$

around $LO_{\parallel}^{1,2}$ in *pac*, whereas

$$\varepsilon_{\perp}(\omega) = \tan^2 \theta, \quad (10b)$$

and

$$\frac{\varepsilon_{\parallel}(\omega) - 1}{\varepsilon_{\perp}(\omega) - 1} \varepsilon_{\perp}(\omega) = \tan^2 \theta, \quad (10c)$$

in *paa* and *pca*, respectively, around LO_{\perp}^{1-4} . We note that in *paa* the BNR appears always just above the frequencies of four S_{\perp}^{1-4} 's, as shown in Fig. 3. For the configurations *pac* and *pca*, on the other hand, the spectral position of a BNR relative to $LO_{\parallel(\perp)}^j$ and/or $S_{\parallel(\perp)}^j$ is determined by the sign and magnitude of $\varepsilon_{\perp(\parallel)}(\omega) \cos^2 \theta$ around $LO_{\parallel(\perp)}^j$. The spectral positions of BNR measured from every LO phonon mode are listed in Table III.

Table III. Position (cm^{-1}) of BNR from the LO phonon specified.

Configuration	LO_{\parallel}^1	LO_{\parallel}^2	LO_{\perp}^1	LO_{\perp}^2	LO_{\perp}^3	LO_{\perp}^4
<i>pac</i>	-0.015	2.23				
<i>paa</i>			< 0.01	0.07	0.01	2.94
<i>pca</i>			0	0.01	< 0.01	4.09

3. Experimental Procedure

Synthetic crystals of sapphire from KYOCERA Corporation are used as the samples. The crystals are

0.33-mm-thick plates with the (0001) or the $(1\bar{1}20)$ faces. They are originally prepared for the use as the substrate for depositing thin films of compound semiconductors.

The SAOIR spectrum is measured using FTIR spectrometers (JASCO FT/IR-410, FARIS-1) with a resolution of 0.5 cm^{-1} . By using an equipment for reflectometry (JASCO RF-81S), the infrared beam coming out of the interferometer of FT/IR-410 or FARIS-1 is folded and focused on the sample crystal at an angle of incidence of 10° . A rotating wire-grid polarizer is placed in front of RF-81S, and the infrared radiation is polarized linearly to be perpendicular (*s*-polarization) or parallel (*p*-polarization) to the plane of incidence. The degree of polarization is greater than 90 % throughout the wavelength region examined. All the experiments are performed at room temperature.

4. Experimental Results and Discussion

Figure 5 shows the experimental results for six principal configurations: In Fig. 5(a) the spectra of *sac* and *pac* are shown, while in Fig. 5(b) and 5(c) the spectra of *sca* and *paa*, and of *saa* and *pca* are shown, respectively. In accord with the preview presented in §2, four reststrahlen bands of E_u modes, rising from TO_{\perp}^{1-4} and ending off at LO_{\perp}^{1-4} , are observed in the former four configurations, and two reststrahlen bands of A_{2u} modes, rising from $TO_{\parallel}^{1,2}$ and ending off at $LO_{\parallel}^{1,2}$, are observed in the latter two configurations.

For all the combinations of *s*- and *p*-spectra, because of the small value of θ there is a strong resemblance between the two spectra over the whole spectral range examined. However, one may notice several definite differences. Namely, a clear dip appears in the *pac* spectrum of Fig. 5(a) around 880 cm^{-1} . It emerges from the preview of Fig. 2 and the BNR spectra observed in GaN¹⁰⁾ and ZnO²¹⁾ that this dip arises from BNR associated with LO_{\parallel}^2 . A more distinct structure is seen from the *c*-plane spectra obtained by Yu *et al.*¹⁸⁾ with larger incident angles $\theta = 16^\circ$ and 45° , consistent with the theory of Kuroda and Tabata²⁰⁾. This BNR appears also in GaN/*c*-sapphire,^{9,10)} since the overlying GaN film is transparent in the relevant frequency region. In addition, compared with four spectra of Figs. 5(a) and 5(b), a deficiency, by about 10 % at most, of *R* of the reststrahlen band of A_{2u}^2 is seen in a region of $680\text{--}820\text{ cm}^{-1}$ of the *saa* and *pca* spectra of Fig. 5(c). The deficiency seems to consist of a few shallow dips. Similar spectra are observed in ZnO/*a*-sapphire

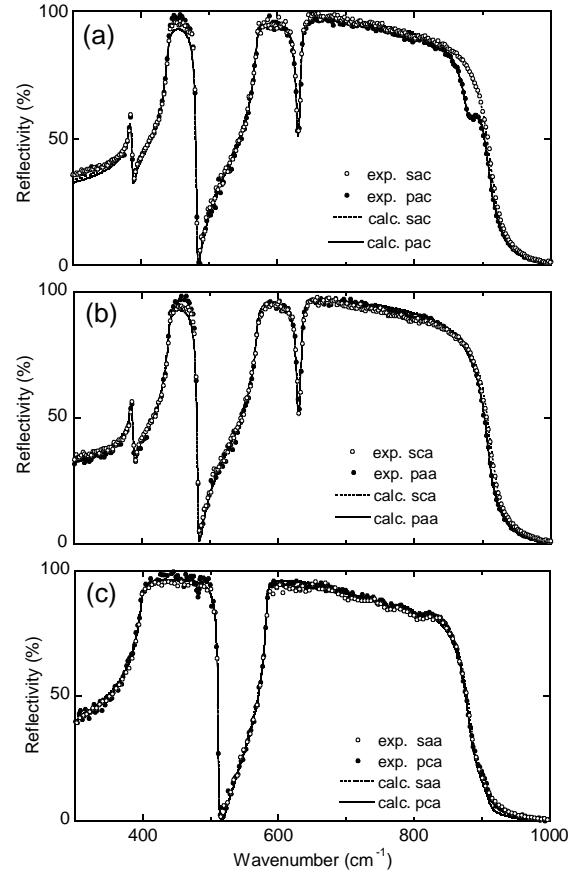


Fig. 5 SAOIR reflectivity of sapphire for the configurations (a) *sac* and *pac*, (b) *sca* and *paa*, and (c) *saa* and *pca*. The open and closed circles are the experimental data for *s*- and *p*-polarized configurations, respectively. The dotted and solid lines are the theoretical curves for *s*- and *p*-polarized configurations, respectively, calculated from the oscillator parameters of Tables I and IV. The dotted lines are hardly visible since they are nearly masked by the marks of the experimental data or superposed on the solid lines. See text.

composites,²⁴⁾ in which thin ZnO films are deposited by molecular beam epitaxy on the sapphire *a*-face of very high quality.²⁵⁾ It is likely, therefore, that weak intrinsic transitions concur with the reststrahlen band of the A_{2u}^2 mode.

To interpret the present observations quantitatively, we calculate the spectra of *R* by introducing nonvanishing damping energies, γ 's, of phonons into the principal dielectric functions given by eq. (3). In view of the above-mentioned deficiency in *R* in the *saa* and *pca* spectra, we add three oscillator terms of $j = 3, 4,$ and 5 to $\epsilon_{\parallel}(\omega)$. Furthermore, we take account of the breadth of the value of θ produced by focusing the infrared beam with a concave mirror of the reflectometry equipment RF-81S mentioned in §3. Since the features of BNR and STR grow up and shift nonlinearly with increasing θ for $\theta \ll 1$,²⁰⁾ in the

precedent work on ZnO we have treated θ as a parameter which should be determined from the experimental data.²¹⁾ In the same way, here we calculate the theoretical curves by adjusting θ as well as the phonon frequencies and damping energies so as to optimally reproduce the experimental spectra. The theoretical curves obtained are shown in Figs. 5(a), 5(b), and 5(c) along with the experimental data. The theoretical curves reproduce the experimental results so well that the theoretical curves are nearly indistinguishable from the symbols of the experimental data points. We obtain $\theta = 10.6^\circ$ with an accuracy of $\pm 0.2^\circ$. This is compared with the value 11.0° taken in the work on ZnO. The distinct contrast between the *a*-face spectra in Figs. 5(b) and 5(c) assures that the degree of the linear polarization of the infrared beam is sufficiently high. In Table I the phonon parameters obtained are listed and compared with relatively recent experimental results of other workers. Table IV gives the parameters of additional oscillators introduced to $\varepsilon_{\parallel}(\omega)$.

Table IV. Frequencies (cm^{-1}) and strengths of weak oscillators observed for configurations *saa* and *pca*. Numbers in parentheses are the dampings (cm^{-1}).

Oscillator number	Frequency		Oscillator strength
	TO mode	LO mode	
3	713 (80)	711 (80)	0.019
4	764 (38)	763 (38)	0.004
5	807 (30)	806 (30)	0.002

Figure 6 shows the enlarged *sac* and *pac* spectra in the region of the shoulder of the E_u^4 band of Fig. 5(a). In addition to the prominent dip due to BNR associated with LO_{\parallel}^2 , the difference between the *sac* and *pac* spectra due to STR just above LO_{\perp}^4 is observed on the higher frequency side of BNR. There also appear the influences of BNR and STR in other configurations. In Fig. 7 the theoretical spectra of differences, $R_{pac}-R_{sac}$, $R_{paa}-R_{sca}$, and $R_{pca}-R_{saa}$, are compared with experimental ones in the frequency region covering LO_{\parallel}^2 and LO_{\perp}^4 . The presence of STR, as well as BNR, in *pac* and *sac* is elucidated by $R_{pac}-R_{sac}$, as shown in Fig. 7(a). To decompose the spectrum into the contributions from BNR and STR the spectra of $R_{pac}-R_{\perp}$ and $R_{\perp}-R_{sac}$ are calculated and shown in Fig. 7(a), where R_{\perp} is the normal-incidence reflectivity for the *c*-face. It turns out that BNR due to LO_{\parallel}^2 and STR due to LO_{\perp}^4 appear as line structures with the center at 881 and 910

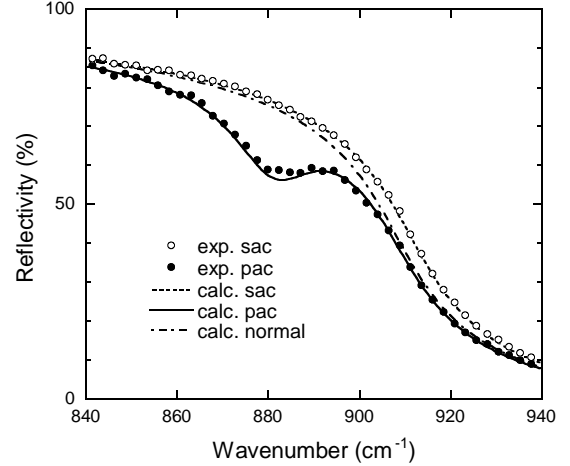


Fig. 6 Close-up around the high-frequency edge of the *sac* and *pac* spectra. The dotted and solid lines are the theoretical curves for configurations *sac* and *pac*, respectively; the dash-dotted line is the theoretical curve of the normal-incidence reflectivity.

cm^{-1} , being just 1.5 cm^{-1} above LO_{\parallel}^2 and LO_{\perp}^4 , respectively. As shown in Fig. 7(b), the BNR structure at the LO_{\perp}^4 edge in *paa*, which was predicted in §2, is observed around 910 cm^{-1} in the form of a line spectrum, as well, in $R_{paa}-R_{sca}$. Corresponding to STR due to LO_{\parallel}^2 in *saa*, and the succeeding STR and BNR due to LO_{\perp}^4 in *pca*, minimum and maximum alternate around 880, 902, and 915 cm^{-1} in the spectrum of $R_{pca}-R_{saa}$, as shown in Fig. 7(c).

Table IV shows a novel relationship of $\omega_{\text{LO}} < \omega_{\text{TO}}$ for the three additional transitions occurring in the configurations *saa* and *pca*. In the present case, these transitions lie in frequency within the TO-LO gap of the A_{2u}^2 mode, and thus the background dielectric constant is negative. Consequently, in the opposite manner to usual polar LO modes the macroscopic field points in the same direction as the polarization of the oscillators. These three additional transitions are so weak that their contributions to $\varepsilon_{\parallel}(\omega)$ of eq.(3) can be rewritten into the sum of classical oscillators to a good approximation. Then, the strengths of the oscillators of $j = 3, 4,$ and 5 emerge to be $0.019, 0.004,$ and 0.002 , respectively, as presented in Table IV. Figure 8 illustrates how these oscillators affect the reststrahlen reflection. The theoretical curves of R_{saa} and R_{pca} shown in Fig. 5(c) are redrawn with thick lines, and the spectra calculated without the additional oscillators are shown with thin lines. The portion of the A_{2u}^2 band of the experimental data for $E_{\parallel}c$ obtained by Barker²⁾ in a fusion crystal of ruby, $\alpha\text{-Al}_2\text{O}_3:\text{Cr}^{3+}$, is also shown for comparison. Apart from the

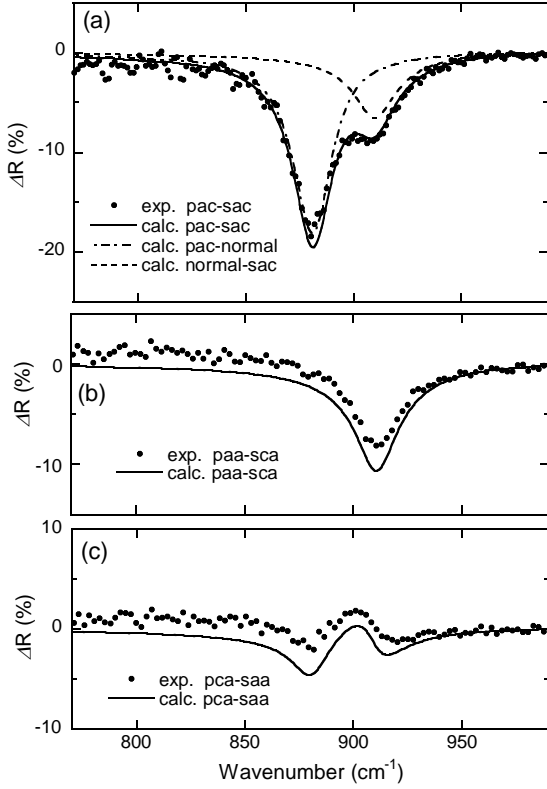


Fig. 7 Experimental (solid circles) and theoretical (solid lines) curves of (a) $R_{pac}-R_{sac}$, (b) $R_{paa}-R_{sca}$, and (c) $R_{pca}-R_{saa}$. The dash-dotted and dashed lines in (a) are the theoretical curves of $R_{pac}-R_{\perp}$ and $R_{\perp}-R_{sac}$, respectively, where R_{\perp} signifies the normal-incidence reflectivity for the c -face of the crystal.

discrepancy in the region of 590-690 cm^{-1} which, according to Barker, can be removed by etching the surface of the sample, the data agree well with the result of the present study. In general, reflectivity is sensitive to small absorption changes in the wing of a strong absorption band. For instance, a multiphonon transition of a summation process appears as a large dip of the reststrahlen band in LiF and MgO.²⁶⁾ In sapphire, the aforementioned D_{3d} point symmetry permits the combination of an infrared active E_u mode and a Raman active E_g mode to be infrared-active for $E \parallel c$. From the present study we have $\omega_{\text{TO}_{\perp}^1} = 384.6 \text{ cm}^{-1}$ and $\omega_{\text{TO}_{\perp}^2} = 439.3 \text{ cm}^{-1}$ for E_u^1 and E_u^2 modes, respectively, whereas E_g modes have frequencies 378 cm^{-1} , 432 cm^{-1} , and so on.²⁷⁾ Let these frequencies be ω_{g1} and ω_{g2} , respectively. Then, $\omega_{\text{TO}_{\perp}^1} + \omega_{g1} = 762.6 \text{ cm}^{-1}$ agrees well with 764 cm^{-1} of the $j = 4$ oscillator; besides, $\omega_{\text{TO}_{\perp}^2} + \omega_{g1} = 817.3 \text{ cm}^{-1}$ and $\omega_{\text{TO}_{\perp}^1} + \omega_{g2} = 816.6 \text{ cm}^{-1}$ are rather close to 807 cm^{-1} of the $j = 5$ oscillator. Furthermore, the multimode phonon dispersion clarified by Kappus²⁷⁾ suggests various possibilities of the combination of phonons

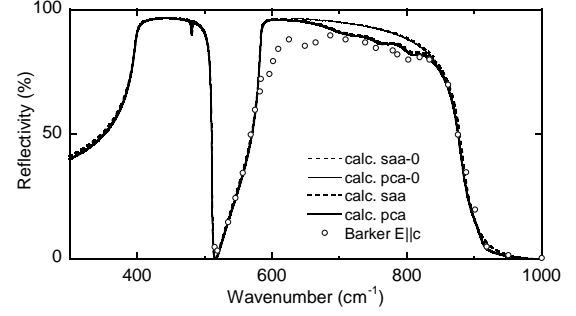


Fig. 8 Influence of additional weak oscillators to the SAOIR reflectivity of sapphire for the configurations *saa* and *pca*. The dotted and solid thick lines are the same theoretical curves as shown in Fig. 5(c), while the thin lines are the theoretical curves calculated without additional weak oscillators. The open circles are the experimental data obtained by Barker from a ruby crystal for $E \parallel c$.

near the surface of the first Brillouin zone. A firm identification must, therefore, await further studies on the properties of the multiphonon states.

Finally, returning our attention to the one-phonon process, we notice a shallow and narrow dip at 481.2 cm^{-1} in the *pca* spectrum of Fig. 5(c). A pronounced narrow dip appears in the same frequency region of an *a*-face spectrum taken by Yu *et al.*¹⁸⁾ with $\theta = 45^\circ$ for a non-principal configuration. We may identify this feature with the damped BNR which was predicted in §2 (see Fig. 4(c)) to occur between LO_{\perp}^2 and S_{\perp}^2 in the *pca* configuration. The experimental spectrum of Fig. 5(c) is reproduced precisely by the theoretical *pca* curve redrawn in Fig. 8. It is comprehensible from Tables II and III that the position of this BNR coincides with LO_{\perp}^2 well.

5. Conclusions

Multimode infrared properties of sapphire have been studied by the small-angle oblique-incidence reflectometry (SAOIR). This is the third article of our SAOIR studies: The precedent works have been reported in Refs. 20 and 21. In the present study we have carried out the theoretical survey on the phonon spectra for all the six principal configurations of the infrared beam relative to the orientation of the birefringent, uniaxial crystal of sapphire. The result has clarified the basic aspects of the influence of Snell's total reflection (STR) and Brewster's null reflection (BNR) upon the reststrahlen bands due to two A_{2u} and four E_u modes of polar optical phonons. STR occurs at frequencies very close to LO phonons in any configurations, whereas BNR takes place near every LO phonon mode polarized normal to the crystal face only in the configurations of *p*-polarization.

The experiment has been conducted for the six principal configurations using *a*- and *c*-face crystals of synthetic sapphire by settling the angle of incidence at 10°. It has turned out that the structures due to STR and BNR specific to SAOIR are superposed on the reststrahlen bands for every principal configuration. The STR and BNR structures are found to show good line structures practically. The spectra have been explained very well in terms of the dielectric function of Gervais and Piriou's four-parameter semi-quantum oscillator model, yielding accurate values of frequency and damping energy of TO and LO phonons. In addition to these one-phonon reflections weak intrinsic transitions due probably to multiphonon processes which are allowed mainly for $E||c$ have been observed in a frequency region of 680-820 cm⁻¹ in the reststrahlen band due to the higher-frequency one of the two A_{2u} modes.

Acknowledgements

The authors Y. K. and N. K. acknowledge IR & Raman Applications Laboratory of JASCO Corporation for their cordial help in the course of the FTIR experiment.

- 1) A. Mitsuishi, H. Yoshinaga, S. Fujita, and Y. Suemoto: Jpn. J. Appl. Phys. **1** (1962) 1.
- 2) A. S. Barker, Jr.: Phys. Rev. **132** (1963) 1474.
- 3) F. Gervais and B. Piriou: J. Phys. C: Solid State Phys. **7** (1974) 2374.
- 4) P. Zu, Z. K. Tang, C. K. L. Wong, M. Kawasaki, A. Ohtomo, H. Koinuma, and Y. Segawa: Solid State Commun. **103** (1997) 459.
- 5) K. Nakahara, T. Tanabe, H. Takasu, P. Fons, K. Iwata, A. Yamada, K. Matsubara, R. Hunger, and S. Niki: J. Appl. Phys. **40** (2001) 250.
- 6) T. Azuhata, T. Matsunaga, K. Shimada, K. Yoshida, T. Sota, K. Suzuki, and S. Nakamura: Physica B **219&220** (1996) 493.
- 7) G. Yu, H. Ishikawa, M. Umeno, T. Egawa, J. Watanabe, T. Soga, and T. Jimbo: Appl. Phys. Lett. **73** (1998) 1472.
- 8) Z. C. Feng, Y. T. Hou, M. F. Li, S. J. Chua, W. Wang, and L. Zhu: Phys. Status Solidi B **216** (1999) 577.
- 9) N. Kuroda, K. Saiki, Hasanudin, J. Watanabe, and M.-G. Cho: AIP Conf. Proc. **772** (2005) 281.
- 10) N. Kuroda, T. Kitayama, Y. Nishi, K. Saiki, H. Yokoi, J. Watanabe, M.-W. Cho, T. Egawa, and H. Ishikawa: Jpn. J. Appl. Phys. **45** (2006) 646.
- 11) J. Chen and W. Z. Shen: Appl. Phys. Lett. **83** (2003) 2154.
- 12) Y. Kumagai, T. Himoto, H. Tampo, H. Yokoi, H. Shibata, S. Niki, and N. Kuroda: AIP Conf. Proc. **893** (2007) 317.
- 13) V. A. Yakovlev, N. N. Novikova, E. A. Vinogradov, S. S. Ng, Z. Hassan, and H. Abu Hassan: Phys. Lett. A **373** (2009) 2382.
- 14) S. S. Ng, S. C. Lee, S. K. Mohd Bakhori, Z. Hassan, H. Abu Hassan, V. A. Yakovlev, N. N. Novikova, and E. A. Vinogradov: Opt. Express **18** (2010) 10354.
- 15) A. K. Harman, S. Ninomiya, and S. Adachi: J. Appl. Phys. **76** (1994) 8032.
- 16) M. E. Thomas, S. K. Andersson, R. M. Sova, and R. I. Joseph: Infrared Phys. Technol. **39** (1998) 235.
- 17) M. Schubert, T. E. Tiwald, and C. M. Herzinger: Phys. Rev. B **61** (2000) 8187.
- 18) G. Yu, N. L. Rowell and D. J. Lockwood: J. Vac. Sci. Technol. A **22** (2004) 1110.
- 19) P. S. Wayland, M. E. Thomas, R. I. Joseph, and M. J. Linevsky: Infrared Phys. Technol. **41** (2000) 307.
- 20) N. Kuroda and Y. Tabata: J. Phys. Soc. Jpn. **79** (2010) 024710.
- 21) N. Kuroda, Y. Kumagai, H. Himoto, and H. Yokoi: J. Phys. Soc. Jpn. **79** (2010) 064712.
- 22) P. Brüesch: *Phonons: Theory and Experiments II* (Springer-Verlag, Berlin, 1986) Appendix B.4.
- 23) J. Lekner: J. Opt. Soc. Am. **A10** (1993) 2059.
- 24) Y. Kumagai: Master Thesis, Graduate School of Science and Technology, Kumamoto University, Kumamoto, Japan (2007) [in Japanese].
- 25) P. Fons, K. Iwata, S. Niki, A. Yamada, K. Matubara, and M. Watanabe: J. Cryst. Growth **209** (2000) 532.
- 26) J. R. Jasperse, A. Kahan, J. N. Plendle, and S. S. Mitra: Phys. Rev. **146** (1966) 526.
- 27) W. Kappus: Z. Physik B **21** (1975) 325.

*Present address: Fuji Electric Device Technology Co., Ltd., Matsumoto Branch, Matsumoto 390-0821, Japan

†Present address: Free Laboratory for Materials Technology, Shimizunuma 2-10-18, Miyagino ward, Sendai 983-0845, Japan

§E-mail address: kurodafmt@ac.auone-net.jp